Construction of dynamic p-n junctions at atomic-scale for unanticipated photocatalytic oxidation activity

Chang Liu [a], Jingze Shao [a], Jinghui Wang [a], Yaowen Wang [a], Yan Wang [b], Zhipeng Fan [a], Liping Li [a,*], Guangshe Li [a,*]

[a] State Key Laboratory of Inorganic Synthesis and Preparative Chemistry, College of Chemistry, Jilin University, Changchun 130026, PR China
[b] Shandong Provincial Key Laboratory of Chemical Energy Storage and Novel Cell Technology, and School of Chemistry and Chemical Engineering, Liaocheng University, Liaocheng 252000, PR China

ARTICLE INFO

ABSTRACT

Dynamic p-n junction can drive a drift of electrons from p-type to n-type side, and that of holes in the opposite direction simultaneously, which offers a promising avenue for next generation of advanced photocatalysts. However, construction of dynamic p-n junctions still remains challenging. Herein, dynamic p-n junctions at atomic-scale are constructed by hybridizing two n-type semiconductors, Zn-doped TiO_2 and P-doped C_3N_4. The catalyst ($Z_{0.01}T/CNP-4$) gives a stable and remarkable photo-oxidation ability for tetracycline hydrochloride (TCH), giving a much higher space-time yield than previously reported. h^+, $^\bullet O_2^-$, and $^\bullet OH$ radicals are main active species for the TCH photo-oxidation. Most importantly, $^\bullet O_2^-$ species react with photo-generated electrons rapidly separated via atomic-level p-n junctions to yield H_2O_2 that further promotes the TCH photo-oxidation process. These findings provide new hints in fabricating more novel dynamic p-n junctions for effectively utilizing both photo-generated electrons and holes in the meanwhile to achieve the full potential of photocatalytic reactions.

1. Introduction

Developing efficient photocatalytic systems is of prime significance for addressing environmental challenges associated with pollutant treatment and remediation [1,2]. Recent efforts have mainly centered on either noble metal-based photocatalysts or semiconductor materials. The latter offer cost-effective alternatives, making them promising for future high-efficiency photocatalysts [3–5]. However, these materials exhibit several detrimental properties, such as wide bandgaps and relatively low quantum efficiency, hampering their practical implementation. Therefore, further development of highly active photocatalysts is of great significance and essential.

Intensive research efforts have been dedicated to elucidating the intricate structure, electrochemistry, and redox mechanisms of photocatalytic systems to enhance the photocatalytic performance of catalysts [6–8]. The catalyst synthesis has evolved from the simple loading of precious metals to the "morphology" or "doping" modification of semiconductor substances, and finally to constructing heterojunctions. Constructing p-n heterojunctions is considered an effective method for

enhancing the performance of hybrid catalysts. For example, a porous core-shell homojunction was constructed by growing amorphous TiO_2 on nonporous rutile TiO_2 crystals, which enhanced the adsorption ability and photoactivity of the catalyst [9]. Tang et al. [10] coupled p-type Bi_2O_3 with n-type Ti^{3+} self-doped TiO_2 porous material to form a novel p-n heterojunction visible light catalyst for tetracycline hydrochloride (TCH) removal. Our recent research [11] on regulating the interface properties of composite catalytic materials has demonstrated that the built-in electric field formed by the p-n junction heterointerface can significantly accelerate the electron transfer in the CO oxidation process. Moreover, the nature of special interfacial chemical bonds not only improves the stability of composite catalysts but also acts as a bridge for transporting electrons [12]. Progress has been made in constructing static p-n junction interfaces. However, the construction of dynamic p-n junctions in the absence of a special synthesis method is challenging, in part due to the characteristic of the electronic structure and the complexity of interfacial lattice that influence the efficiency of charge separation and subsequent catalytic reactions.

Brookite TiO_2 has garnered increasing attention in the field of

photocatalysis and solar cell applications due to its optimal defect depth [13,14]. Research has shown that defects in TiO_2 can capture electrons, thereby extending the lifetime of photo-generated charge carriers [15]. However, challenges still exist, including limited light absorption range and catalyst stability of TiO_2. To address these issues, many strategies, such as ion doping and the construction of heterocomposite, have been adopted to modulate the band structure of TiO_2, aiming to broaden the light absorption range of the catalyst [16]. Two-dimensional polymer C_3N_4 has the advantages of cost-effectiveness, facile synthesis, and environmental compatibility, being a prominent candidate in photocatalytic pollutant removal [17,18]. Although a combination of C_3N_4 with semiconductor oxides to form heterocomposite (e.g., C_3N_4/TiO_2 [19], P-doped C_3N_4/SnO_2 [12]) improves photocatalytic efficiency partly, debates remain in the understanding of how these composites interact with diverse reactants, particularly concerning the in-situ formation of atomic-scale heterojunctions during photocatalysis-driven redox reactions.

In this work, a series of photocatalysts with in situ built dynamic p-n junctions at atomic-scale were synthesized by hybridizing Zn-doped brookite TiO_2 and P-doped C_3N_4 (CNP) via the rapid thermal quenching process. In free of electron sacrificial agent, the optimal catalyst $Z_{0.01}T/CNP$-4 effectively oxidized tetracycline hydrochloride (TCH) under visible light and gave the highest space-time yield ever reported. Spectroscopy and photo-electrochemical studies as well as density functional theory calculations prove that the forming of dynamic p-n junctions at the atomic-scale enhance charge separation and transportation. Free radical trapping experiments and electron-spin resonance (ESR) data analysis further demonstrated that $^\bullet O_2^-$, h^+, and $^\bullet OH$ radicals were the main active species during the photocatalytic reaction process. The hydrogen peroxide generated by the reaction between photogenerated electrons and free radical $^\bullet O_2^-$ further promotes the TCH oxidation. This study showcases an innovative concept for efficiently constructing in-situ catalysts with p-n junction interface, which can effectively utilize photogenerated electrons and holes for efficient chemical reactions, overcoming the limitation of traditional photocatalysis.

2. Experimental section

2.1. Catalyst preparation

2.1.1. Synthesis of P-doped C_3N_4

P-doped C_3N_4 (CNP) was synthesized according to our previous work [12]. Briefly, melamine and 2-aminoethyl phosphoric acid were added to 50 mL of water and stirred to dryness. The dried powder was calcined at 500 °C for 3 h and 550 °C for another 3 h in flowing N_2. The calcined product was thoroughly ground and then annealed again in a muffle furnace at 550 °C for 3 h to obtain brown P-doped C_3N_4 (Fig. S1). The atom ratio of C:N is nearly 2.5:4 by the element analysis, and that of P:N is 1:32 by EDS. Control sample C_3N_4 (CN) was also prepared using the same procedure, except that no phosphorus source was added.

2.1.2. Synthesis of Zn-doped TiO_2

Firstly, brookite TiO_2 nanocrystals were synthesized via hydrothermal method. In more detail, 40 mL of deionized water was cooled for 15 min in an ice-water bath. Then, 1.5 mL of $TiCl_4$ solution was slowly added dropwise and stirred for 30 min. Next, 5.0 g of urea and 8.0 mL of DL-sodium lactate were added in batches, respectively. The final mixture was placed in a 100 mL Teflon-lined stainless-steel autoclave and heated at 200 °C for 24 h. After cooling down, a solid was obtained and ground into a fine powder. The powder was calcined at 500 °C for 1 h to remove surface adsorbed substances (H_2O, solvent, et.al), as shown in Fig. S2. The obtained sample is phase-pure brookite TiO_2 nanocrystals, as confirmed by XRD and Raman spectrum analysis (Fig. S3). For convenience of expression, the phase-pure brookite TiO_2 nanocrystals are called TiO_2 in the following description.

Brookite TiO_2 has exhibited a special interaction with zinc oxide [20], which could help forming Zn-doped brookite TiO_2 nanocrystals at low temperature. Thus, a combination of co-precipitation reaction and annealing processes is designed to synthesize Zn-doped TiO_2 samples that a key reaction precursor for building ZT/CNP nano-hybrids. Taking $Zn_{0.01}Ti_{0.99}O_2$ (the target mole ratio of Zn to Ti is 0.01) as an example, 0.5 g TiO_2 and 0.017 g of zinc nitrate hexahydrate were placed in 50 mL of ethanol solution, ultrasonically dispersed for 10 min. The suspension was placed in a 50 °C water bath and kept stirring until dry. The dried powder was annealed in a Muffle furnace at 400 °C for 2 h to obtain sample $Zn_{0.01}Ti_{0.99}O_2$. Using the same synthesis procedures, the sample $Zn_{0.03}Ti_{0.97}O_2$ with mole doping content of Zn is 0.03 was also synthesized by adjusting the additional amount of zinc nitrate hexahydrate.

2.1.3. Synthesis of ZT/CNP samples

0.1 g of $Zn_{0.01}Ti_{0.99}O_2$ and 0.4 g of CNP samples were put into 50 mL of ethanol solution and stirred overnight until dry. This process is very important for the effective contact of $Zn_{0.01}Ti_{0.99}O_2$ and CNP with the opposite Zeta potentials (Fig. S4). The mixed powder was annealed in a muffle furnace at 500 °C for 1 h and then quenched to liquid nitrogen. The obtained sample was named $Z_{0.01}T/CNP$-4, in which $Z_{0.01}T$ represents $Zn_{0.01}Ti_{0.99}O_2$, and the number "– 4″ denotes that the mass ratio of CNP to Zn doped TiO_2 equals 4. Using the similar procedure, samples $Z_{0.01}T/CNP$-2, and $Z_{0.01}T/CNP$-6 as well as $Z_{0.03}T/CNP$-4 were also obtained.

2.2. Characterizations

Powder X-ray diffraction patterns (XRD) were collected using a Riraku Miniflex instrument equipped with Cu-Kα radiation (λ = 0.15418 nm), operated at 40 kV and 15 mA, with a scanning range of 2θ= 10–80°. XRD data with Nickel powder as the internal standard for peak position calibration were refined by Rietveld analysis using GSAS program to determine their lattice parameters. Scanning electron microscope (SEM) images were captured using a JSM-6700 F equipment. Energy dispersive spectroscopy (EDS) was performed in SEM mode to acquire data revealing the respective compositions. Transmission electron microscopy (TEM) images were recorded with a Tecnai G2S-TwinF20 instrument. Nitrogen absorption and desorption measurements were carried out on an ASAP2420 instrument. Prior to measurement, all samples were subjected to degassing at 80 °C for 2 h. Ti L-edge and O K-edge XAS measurements were conducted using a waveguide diffraction monochromator (SGM). X-ray photoelectron spectra (XPS) of the samples were obtained using an ESCALAB250 instrument equipped with an Al Kα monochromatic beam. Raman data were recorded using a Raman spectrometer (inVia) with a laser beam of 532 nm. Photoluminescence (PL) spectra were acquired using an Edinburgh Instruments FLS920 spectrometer, with a 450 W xenon lamp as the excitation source. The equipment for the detection of surface photovoltage (SPV) spectrum consists of a 500 W Xenon lamp (CHF-XM-500 W), a monochromator (ZLolix SBP500), a lock-in amplifier (SB830-DSP) coupled with a light chopper (SR540) and interfaced with a computer. The testing frequency was set at a constant 24 Hz, and the wavelength scanning spanned from 300 to 800 nm.

2.3. Performance evaluation

The photocatalytic activities of samples were tested in a customized photochemical reactor under visible light irradiation (λ > 400 nm). In a typical reaction, 20 mg of photocatalyst is added to 50 mL of TCH solution (20 mg/L). The solution was stirred in the dark for 30 min to achieve adsorption equilibrium. The cooling water circulation temperature was set at 20 ± 2 °C during the photooxidation test. During illumination, 2 mL suspension was removed from the reactor at fixed intervals and filtered with a 0.22 μm membrane to separate the photocatalyst. The concentration of TCH was determined by UV–vis

spectrophotometry. After spectrum was recorded, the TCH solution was put back into the reaction solution. Such operations must be done as quickly as possible.

The space-time yield of the catalyst was obtained by calculating the quantum efficiency.

$$Quantum\ efficiency = \frac{Degradation\ rate(molecules\ per\ second)}{Photon\ flux(photons\ per\ second)} \quad (1)$$

$$Space\ time\ yield = \frac{Quantum\ efficiency(molecules\ per\ photon)}{Photocatalyst\ mass(g)} \quad (2)$$

In our experiment, the irradiation area was 1.69 cm^2 and the photon flux was measured by the optical power meter (Thorlabs).

The production of H_2O_2 during the photooxidation experiment were tested in a customized photochemical reactor under visible light irradiation ($\lambda > 400$ nm). 20 mg of photocatalyst was added to the TCH solution (50 mL, 20 mg/ L). The solution was stirred in the dark for 30 min to achieve adsorption equilibrium. The concentration of H_2O_2 was measured by the colorimetric method using DPD [21]. The specific process is as follows: 300 μL mixture solution of Na_2HPO_4 (0.01 M) and NaH_2PO_4 (0.09 M), 30 μL solution of DPD (10 mg/mL), and 30 μL solution of peroxidase (1 mg/mL) was added to deionized water (3 mL), successively. Then, 1 mL of the filtrate was added to the mixed solution. Finally, the absorbance at 553 nm was measured by a UV–vis spectrometer to estimate the amount of H_2O_2 production.

The cycling stability of catalyst $Z_{0.01}T/CNP-4$ was tested under 300 W xenon lamp irradiation ($\lambda > 400$ nm) for 20 min. After each cycle, the photocatalyst was thoroughly washed and dried. The catalysts were collected and weighed for the next test.

2.4. Electrochemical measurements

A three-electrode test system equipped with an electrochemical workstation (CHI 760E) was employed to evaluate the photoelectrochemical properties of the samples in a 0.5 M Na_2SO_4 aqueous solution. The working electrode consisted of spin-coated catalysts on FTO (SnO_2: F), while platinum foil and Ag/AgCl electrodes were utilized as the counter electrode and reference electrode, respectively. Electrochemical impedance spectra (EIS) were recorded at a fixed voltage of 0.1 V. Photocurrent-time (I-t) curves were measured using a 300 W Xenon lamp with an illumination power of 100 mW·cm^{-2}, coupled with a cut-off filter > 400 nm.

2.5. Theoretical calculation method

All the density functional theory (DFT) calculations can be found in Supporting Information.

3. Results and discussion

3.1. Synthesis and structural characterizations of hybrids ZT/CNP

ZT/CNP nano-hybrids were successfully constructed by a multi-step in-situ method, as described in the Experimental Section. XRD patterns of samples $Zn_xTi_{1-x}O_2$ in Fig. S3a confirm the formation of brookite TiO_2 (JCPDS 76–1935) [22], and no obvious diffraction peaks of Zn compounds are observed. The Raman spectra in Fig. S3b do not show the characteristic signals of anatase (at 399 and 519 cm^{-1}) and rutile (at 447 and 612 cm^{-1}), further evidencing the as-obtained samples $Zn_xTi_{1-x}O_2$ are phase-pure brookite [23], in good agreement with the XRD analysis. The A_{1g} band of $Zn_xTi_{1-x}O_2$ is redshifted with Zn doping. Moreover, the lattice parameters of $Zn_xTi_{1-x}O_2$ also slightly increase with *x*, as an illustration of Rietveld refinement for $Zn_xTi_{1-x}O_2$ (Fig. S4 and Table S1), due to the larger ionic radius of Zn^{2+} (0.74 nm) comparing to that of Ti^{4+} (0.0605 nm).

The XRD patterns of the ZT/CNP catalysts are depicted in Fig. S5a-b.

In addition to the diffraction peak of brookite TiO_2, two peaks at 12.9° and 27.4° belong to (100) and (002) diffractions of CNP. Moreover, the (002) diffraction of CNP and (210) diffraction of brookite TiO_2 for sample $Z_{0.01}T/CNP-4$ shift to high angle compared to that of CNP and $Zn_{0.01}Ti_{0.99}O_2$, as shown in Fig. S5b. Large shift of (002) diffraction indicates a lattice contract. As listed in Table S1, the cell volume of the CNP component in $Z_{0.01}T/CNP-4$ is 93.75 $Å^3$, much smaller than 95.93 $Å^3$ of pure P-doped C_3N_4 (CNP), due to severe *a*-axis shrinkage caused by hybridization. The presence of strong interfacial interaction between $Zn_{0.01}Ti_{0.99}O_2$ and CNP leads to the lattice contract of CNP and changes the state of the surface charge of $Z_{0.01}T/CNP-4$ (Fig. S6). Component TiO_2 does not give an obvious lattice shrinkage as that of CNP, which should be related to a large bulk elastic modulus of brookite TiO_2. TEM measurements indicate that Zn-doped brookite TiO_2 consists of nanoparticles (Fig. S7a-b), and tiny $Zn_{0.01}Ti_{0.99}O_2$ particles are tightly dispersed on the surface of the CNP nanosheets (Fig. S7c-d). Lattice fringes with space of 0.35 nm and 0.27 nm observed in the high-resolution TEM (HRTEM) image (Fig. S7e-f) are assigned to the (210) and (020) planes of the brookite TiO_2. The elemental mapping results (Fig. S8) of the $Z_{0.01}T/CNP-4$ composite demonstrate the presence of C, N, O, P, Ti, and Zn elements, and they distribute homogeneously.

XPS was employed to comprehensively characterize the compositions and surface chemical states of as-synthesized samples. The survey XPS spectra of ZT/CNP samples (Fig. S9) reveal the presence of abundant C, N, Ti, and O, as well as a small amount of Zn, consistent with elemental mapping (Fig. S8). We checked Zn 2p and Ti 2p binding energy difference with O 1 s (ΔE_b), as denoted in Fig. 1c. Strong interfacial interaction between $Zn_{0.01}Ti_{0.99}O_2$ and CNP gives rise to an obvious decrease of binding energy difference of Zn $2p_{3/2}$ and O 1 s. Decreased value of ΔE_b between O 1 s and Ti $2p_{3/2}$ for sample $Z_{0.01}T/CNP-4$ suggests an enhanced covalent Ti-O bond due to electron transfer from CNP to $Zn_{0.01}Ti_{0.99}O_2$, which can improve its activity in photocatalytic reactions.

The X-ray absorption near-edge structures (XANESs) of Ti L-edge and O K-edge (Fig. 1d-f) were utilized to analyze the average chemical state and elucidate the influence of local structure on surface oxygen sites. Four peaks, α, β, γ, and δ, in the Ti L-edge XANES spectra (Fig. 1f), correspond to the Ti 3d (L_1) and Ti 3d (L_2) orbitals. Peaks marked as "a" and "b" in O K-edge XANES (Fig. 1g) attributed to the orbital hybridization of Ti 3d and O 2p, peak "c" arises from the antibonding σ* states formed by oxygen-oxygen 2p interactions, and peak "d" are associated with the orbital hybridization of Ti 4sp and O 2p. All the white lines of Ti L-edge and O K-edge peaks of composite $Z_{0.01}T/CNP-4$ are lower than that of $Zn_{0.01}Ti_{0.99}O_2$. Orbital vacancy of $Z_{0.01}T/CNP-4$ is reduced due to electron transfer from CNP to $Zn_{0.01}Ti_{0.99}O_2$, similar to our previous researches [24,25] and reference reports [2]. The lower intensity of the white line peak in $Z_{0.01}T/CNP-4$ supports that the activated surface oxygen sites of hybrid possess a high electron density. Intense EPR signal observed at g= 2.002 for $Z_{0.01}T/CNP-4$ (Fig. 1h) comes from two parts of unpaired electrons: localized in the CNP (V_N •) and in the oxygen vacancies that capture one electron to form V_O •. The former is associated with the unpaired electrons of sp^2-carbon atoms in the π-conjugated aromatic rings [26], and the latter is highly dependent on the oxygen vacancies in the TiO_2 [27,28]. In other words, hybridizing between $Zn_{0.01}Ti_{0.99}O_2$ and CNP yields more reactive oxygen sites. The enhanced covalence in the Ti−O bonds, strong interfacial interaction, and electron transfer between TiO_2 and CNP, as indicated by the combined analysis of XPS, XANES, and EPR, is closely related to the formation of the p–n junctions.

3.2. Evidences of p–n junctions in the hybrid ZT/CNP

Density functional theory (DFT) calculations were first conducted to gain a deeper understanding of the electronic structure in the $Z_{0.01}T/CNP$ sample. As displayed in the density of states (DOS) of $Z_{0.01}T/CNP$ (Fig. 2a), the valence band below the Femi level is mainly contributed by
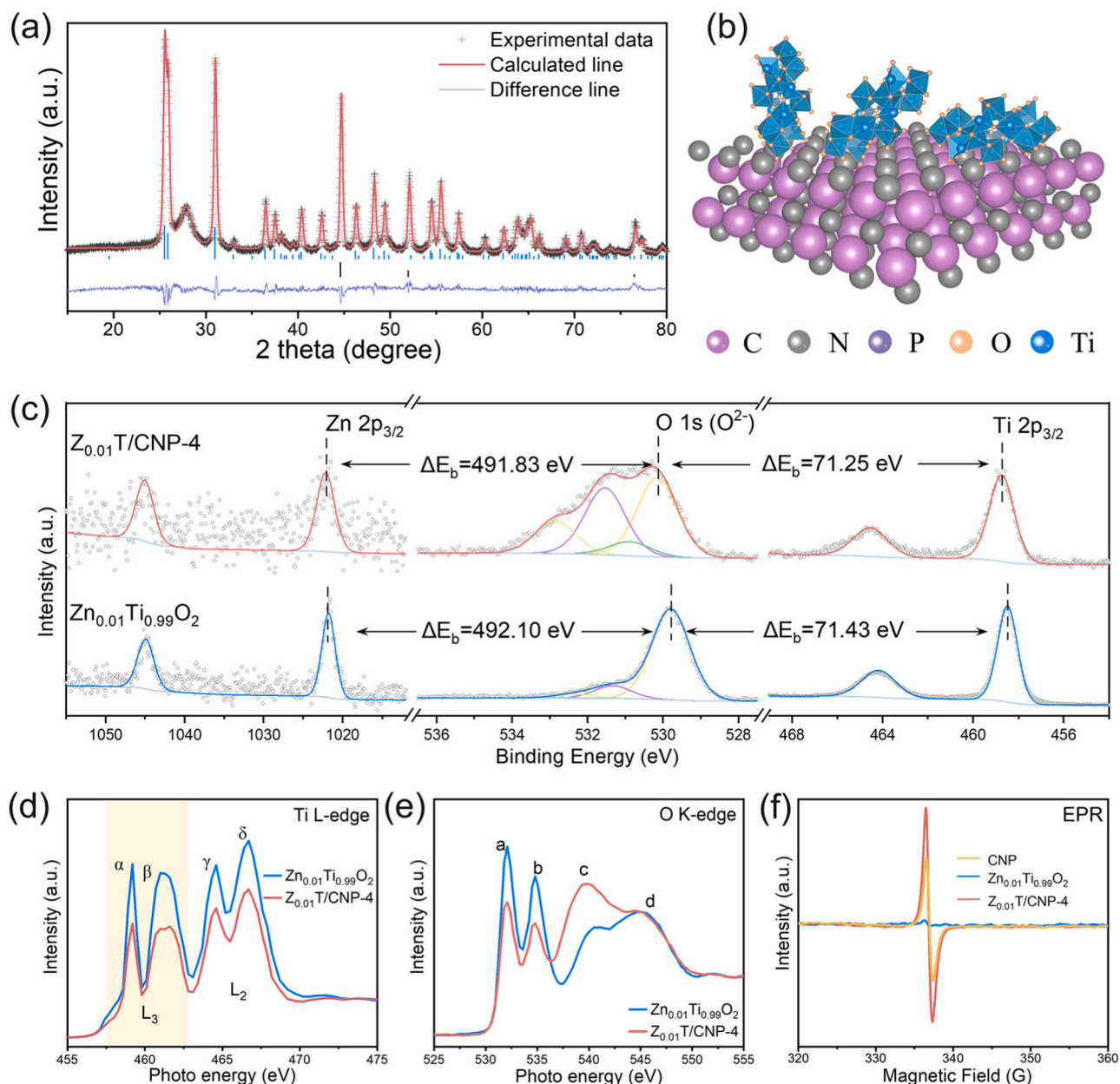
Fig. 1. Characterization of catalysts. (a) Rietveld refinement of XRD pattern and (b) schematic illustration of sample $Z_{0.01}T/CNP$-4. (c) High-resolution Zn 2p, O 1 s, and Ti 2p XPS spectra, (d) Ti L-edge and (e) O K-edge XANES of samples $Zn_{0.01}Ti_{0.99}O_2$ and $Z_{0.01}T/CNP$-4. (f) EPR spectra of samples CNP, $Zn_{0.01}Ti_{0.99}O_{2,}$ and $Z_{0.01}T/CNP$-4.

N atoms and O atoms, and the conduction band above the Femi level is mainly composed of Ti atoms and C atoms. An obvious band gap indicates that $Z_{0.01}T/CNP$ is a typical semiconductor. The UV–vis diffuse reflection spectra (Fig. 2b) confirm that $Z_{0.01}T/CNP$-4 exhibits semiconductor characteristics and has a broad light absorption range. For a comprehensive understanding of the electronic structure and chemical behavior of $Z_{0.01}T/CNP$, we calculated the charge density difference, as shown in Fig. 2c. The charge accumulation and the charge depletion lead to charge redistribution at the interface of $Zn_{0.01}Ti_{0.99}O_2$ and the CNP. Such redistribution and transfer of charge are beneficial to enhancing the adsorption and catalytic reaction on the catalyst surface. Our previous researches have shown that the formation of unique chemical bonds at the interface of metal oxide hybrid CNPs can accelerate electron transfer [12,29]. Fig. 2d displays the ^{31}P MAS NMR spectrum. Different from CNP, four signals can be identified in the spectrum of $Z_{0.01}T/CNP$-4. Three signals Q_0, Q_2, and Q_3 correspond to P

doping at the angular and bent carbon positions of C_3N_4, while Q_1 comes from interface chemical bond P-O-Ti/Zn, similar to our previous findings [29]. The P-O-Ti/Zn bond between P and the central metal ions leads to a redistribution of electron density, weakening the bonding effect between the central ion and the titanium-based oxygen ligand. Therefore, the oxygen atoms of the titanium group have a higher negative charge and are more active in intermolecular interactions. Notably, $Z_{0.01}T/CNP$-4 exhibits significant signal broadening (Q_0), which may be attributed to the existence of different nuclear spin environments inside the hybrid catalyst.

The Mott-Schottky curve is a well-established method to determine the semiconductor type. Generally, n-type semiconductor gives a positive slope in the Mott-Schottky plot, while p-type semiconductor has a negative slope [30]. Mott-Schottky curves of CNP, $Zn_{0.01}Ti_{0.99}O_2$, and ZT/CNP-4 are compared in Fig. 2e and Fig. S10. Both samples $Zn_{0.01}Ti_{0.99}O_2$ and CNP have positive slope, indicative of their n-type
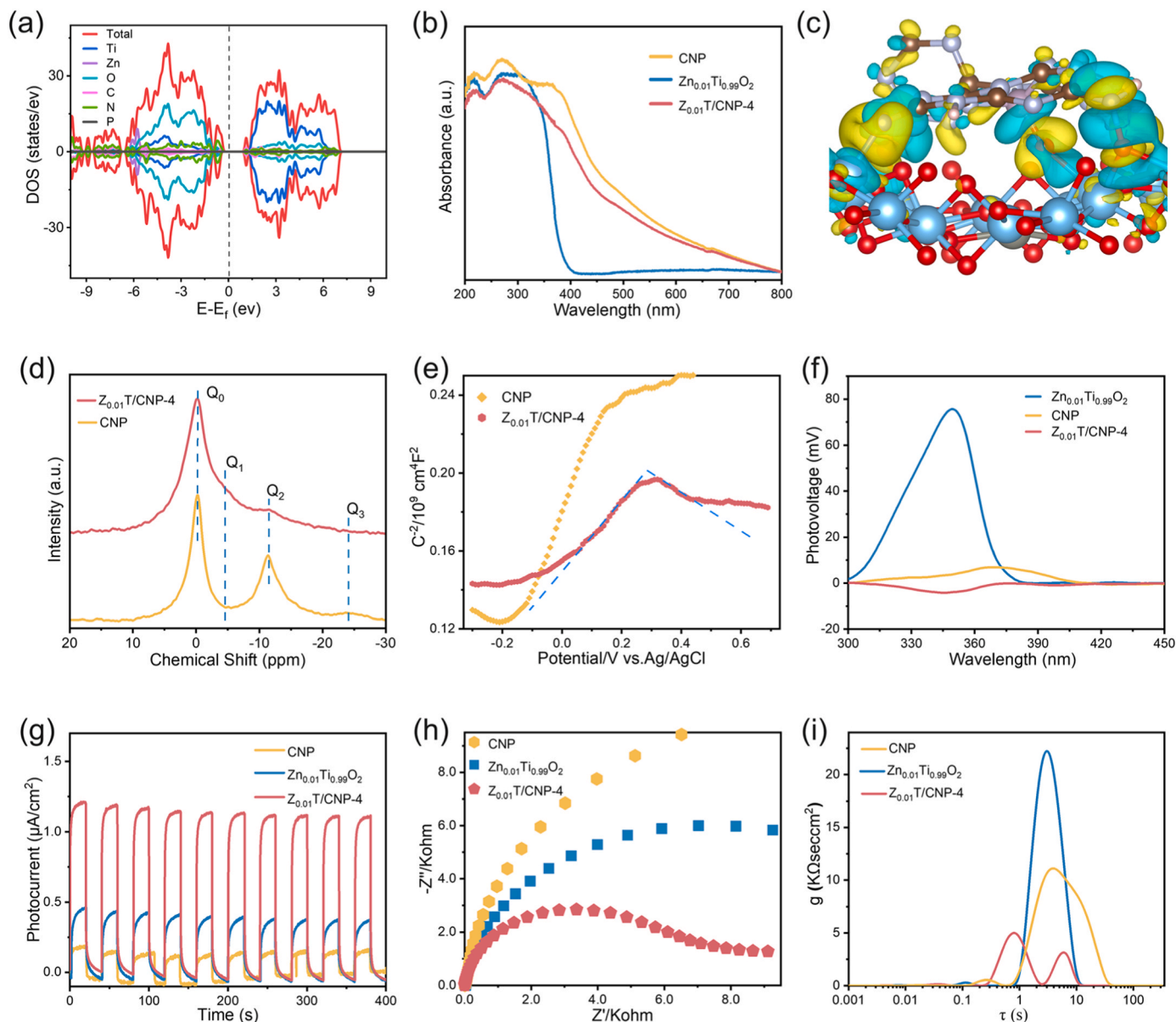
Fig. 2. Results of density functional theory calculation and photoelectrochemical properties. (a) Distributions of state densities. (b) UV–vis diffuse reflection spectra of samples CNP, $Zn_{0.01}Ti_{0.99}O_2$, and $Z_{0.01}T/CNP-4$. (c) Charge density difference maps. Yellow and cyan indicate the electron's accumulation and depletion, respectively. (d) ^{31}P MAS NMR spectra, and (e) Mott-Schottky plots of samples CNP and $Z_{0.01}T/CNP-4$. (f) SPV spectra, (g) transient photocurrent response curves, (h) EIS Nyquist plots and (i) their corresponding DRT of samples CNP, $Zn_{0.01}Ti_{0.99}O_2$, and $Z_{0.01}T/CNP-4$.

semiconductor feature. Different from the observation for $Zn_{0.01}Ti_{0.99}O_2$ and CNP, $Z_{0.01}T/CNP-4$ shows an inverted "V-type" curve with a combination of positive and negative slopes in various potential regions (Fig. 2e), which reveals a coexistence of n-type and p-type domains [31, 32]. It should be mentioned that $Z_{0.01}T/CNP-6$, $Z_{0.01}T/CNP-2$, and TO/CNP-4 do not show obvious "V-type" Mott-Schottky curves and are mainly n-type semiconductors. Unique p-type characteristics of sample $Z_{0.01}T/CNP-4$ may originate from the nitrogen-cavitated $g-C_3N_4$ domain, while the n-type characteristics of other samples might be related to their having much more $g-C_3N_4$ domains with ordered structure. Forming such a special nitrogen-cavitated $g-C_3N_4$ domain can also explain the pronounced broadening of the Q_0 signal in the ^{31}P MAS NMR spectrum (Fig. 2d).

To confirm the coexistence of n-type and p-type domains in the sample $Z_{0.01}T/CNP-4$, surface Photovoltage (SPV), widely used to characterize the carrier separation dipole [33,34], was measured for samples $Z_{0.01}T/CNP-4$, $Zn_{0.01}Ti_{0.99}O_2$ and CNP. As well known, due to

the presence of the surface space charge region (SCR), n-type semiconductors typically exhibit a positive SPV signal, while p-type semiconductors show the opposite SPV signal. Upon light excitation, both samples $Zn_{0.01}Ti_{0.99}O_2$ and CNP exhibit positive SPV (Fig. 2f), consistent with their n-type semiconductor characteristics, as reported in the literature [35]. Different from $Zn_{0.01}Ti_{0.99}O_2$ and CNP, $Z_{0.01}T/CNP-4$ sample shows a weak negative SPV signal, indicating that more photogenerated holes can accumulate on the surface. This observation confirms that the transport of photo-generated carriers is changed due to the presence of built-in p-n junctions at the atomic scale in the $Z_{0.01}T/CNP-4$ catalyst. The co-existence of n- and p-type domains could form p-n junctions, thus creating a built-in electrical field at the junction interface [35–37]. Such built-in electrical fields enable the photo-generated electrons and holes to migrate in opposite directions and effectively improve their separation efficiency.

The formation of p-n junctions at atomic scale can effectively improve photogenerated carrier separation, which can be understood by

a combined analysis of photoluminescence (PL) spectra, transient photocurrent response (I-t) curve, Nyquist plots of electrochemical impedance spectroscopy (EIS), and distribution of relaxation times (DRT). As depicted in Fig. S11, sample $Z_{0.01}T/CNP-4$ exhibits lower PL intensity compared with CNP photocatalysts. The charge recombination rate of $Z_{0.01}T/CNP-4$ is reduced due to the existence of p-n junctions. Fig. 2g compares the I-t curve of $Z_{0.01}T/CNP-4$ with the other two control samples. Notably, $Z_{0.01}T/CNP-4$ displays the highest photocurrent response, approximately 2.9 times higher than $Zn_{0.01}Ti_{0.99}O_2$ and 9.4 times higher than CNP. Besides, the smallest diameter of the Nyquist circle observed for $Z_{0.01}T/CNP-4$ (Fig. 2h) evidences its greatly enhanced charge transfer efficiency. Steady and rapid transport of photogenerated carriers of $Z_{0.01}T/CNP-4$ are also confirmed by DRT analysis as it shows lower intensity of DRT peaks (Fig. 2i). These results indicate that p–n junctions can achieve low charge recombination and efficient separation and transfer, which are crucial for improving the photocatalytic activity of ZT/CNP catalysts.

3.3. TCH photooxidation performance

The catalytic performance of ZT/CNP photocatalysts was evaluated by the photocatalytic oxidation of antibiotic-contaminated wastewater. TCH photooxidation reaction rates and efficiencies of catalysts are compared in Fig. 3a-b and Fig. S12. Poor photooxidation activity of $Zn_{0.01}Ti_{0.99}O_2$ is related to its narrow light absorption range (Fig. 2c), and that of CNP to the rapid recombination of electron-hole pairs. Comparatively, sample $Z_{0.01}T/CNP-4$ exhibits an enhanced TCH photooxidation efficiency, reaching 82% under identical conditions. Moreover, sample $Z_{0.01}T/CNP-4$ gives the highest apparent rate constant (K) that was obtained from the pseudo-first-order kinetics analysis of

ZT/CNP photocatalysts (Fig. 3c, Fig. S13, and Table S2-3).

Space-time yield is widely used to quantify the photocatalytic activity of catalysts. The calculation of space-time yield needs to consider the factors of catalyst dosage, pollutant concentration, irradiation duration, and applied power of irradiation light [38]. The calculated space-time yield of $Z_{0.01}T/CNP-4$ is about 18.5, higher than the well-known catalysts reported in references (Fig. 3d and Table S2). In-situ built p–n junctions furnish catalyst $Z_{0.01}T/CNP-4$ a superior TCH photooxidation activity.

The pH value of the TCH solution significantly influences the surface properties of the catalyst and the formation of reactive species in the photooxidation reaction. The photocatalysts, applied in the photocatalytic removal of TCH, suffer from shortcomings of the narrow applicable pH range [39]. pH value dependent activities of $Z_{0.01}T/CNP-4$ are shown in Fig. 4a. The photooxidation efficiency of $Z_{0.01}T/CNP-4$ is slightly inhibited at strong acid conditions (pH=2). In acidic conditions, a high concentration of H^+ ions can capture $^{\bullet}OH$ and $^{\bullet}O_2^-$ radicals, crucial species for TCH photooxidation. When the pH value changes from 5 to 11, the efficiency slightly increases and then decreases. Compared with the photocatalysts and Fenton-like catalysts reported in the literatures, catalyst $Z_{0.01}T/CNP-4$ exhibits favorable TCH removal performance over a wide pH range under the irradiation of visible light.

Many inorganic ions and natural organic matter in real water systems can affect the photooxidation efficiency of TCH [40]. Fig. 4b shows the photooxidation efficiency of TCH in the presence of different co-existing ions. When NaCl or $CaCl_2$ is added to the reaction solution, but other reaction conditions remain the same, TCH photooxidation efficiency can still reach up to 78 ~ 80%. Monovalent cations (Na^+) had a relatively weak impact on photocatalytic reduction efficiency compared to
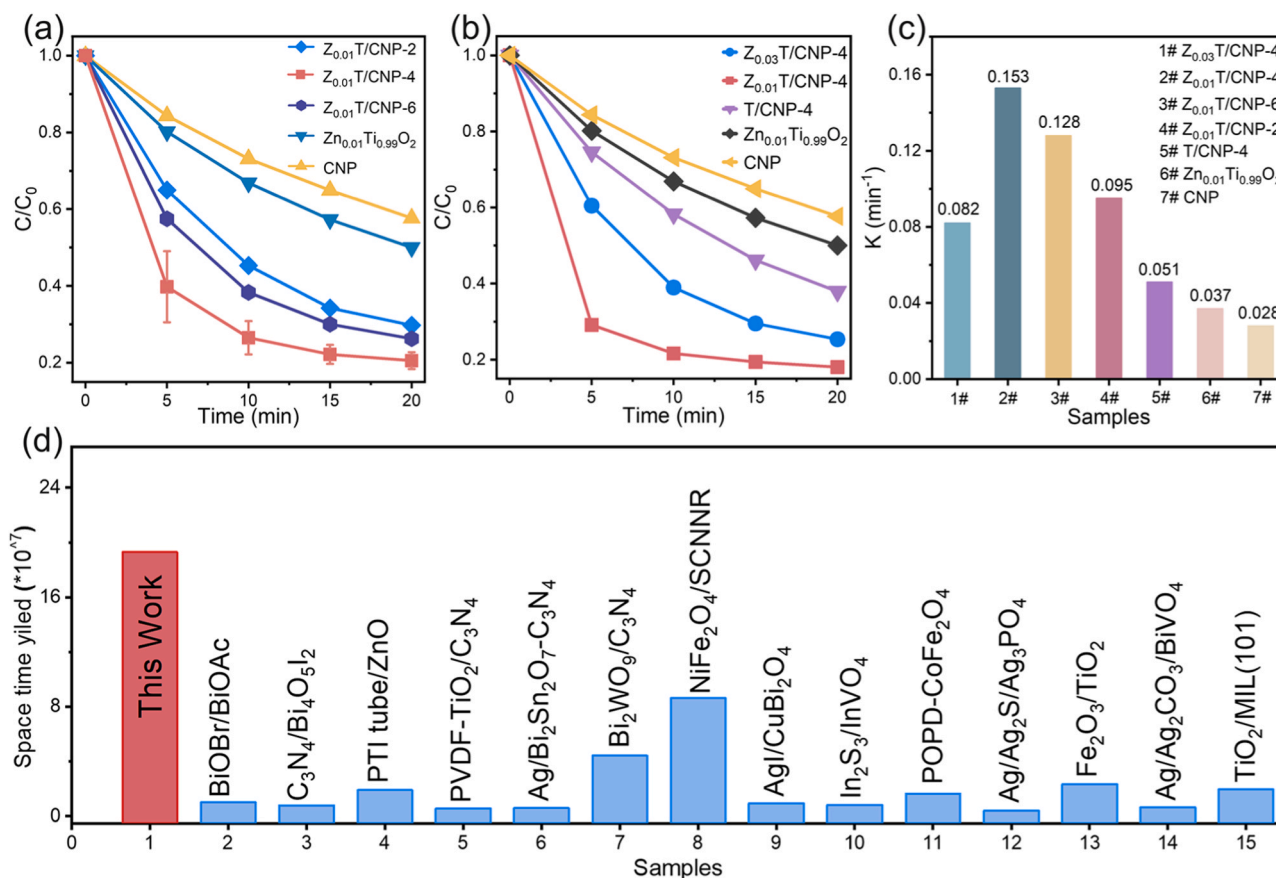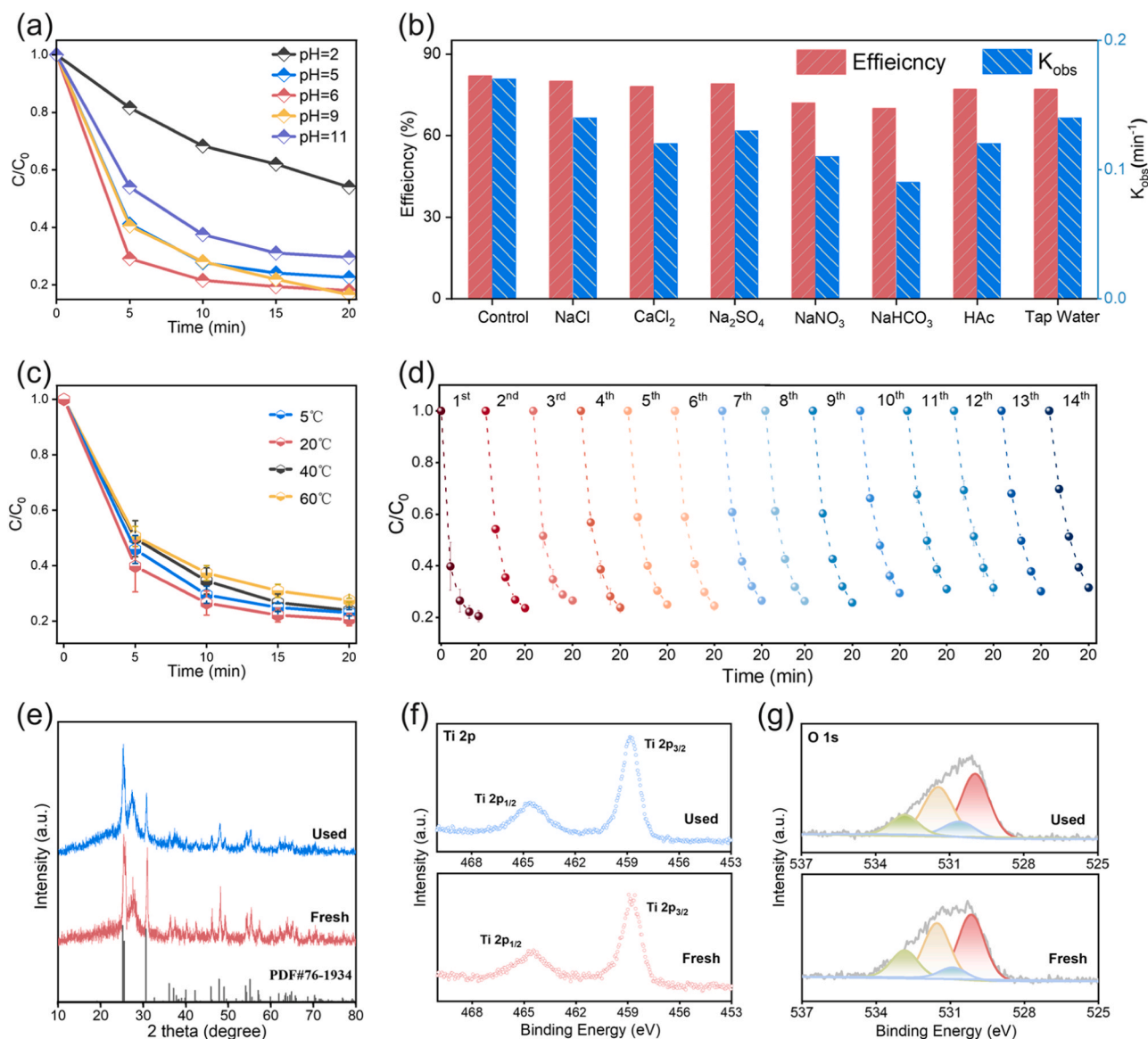

Fig. 3. Photooxidation performance of tetracycline hydrochloride. (a and b) Photooxidation efficiency of TCH under different residence times, and (c) the apparent rate constant for different samples. (d) Comparison of TCH photooxidation space-time yield between the sample $Z_{0.01}T/CNP-4$ and other catalysts reported.

Fig. 4. Adaptability, stability, and reusability. (a) Change of TCH relative concentrations with time in different pH solutions. (b) Photooxidation efficiency of TCH in the presence of co-existing ions. (c) Change of TCH relative concentrations with time at different testing temperatures. (d) Cycling performance of $Z_{0.01}T/CNP$-4 for TCH photooxidation. A comparison of (e) XRD patterns and core level XPS spectra of (f) Ti 2p and (g) O 2p of fresh and used $Z_{0.01}T/CNP$-4 samples.

divalent cations (Ca^{2+}). Divalent cations can potentially adsorb onto the photocatalyst surface's active sites, leading to inhibition of both adsorption and photocatalytic activities. The presence of Cl^-, NO_3^-, SO_4^{2-}, HCO_3^-, and acetic acid (HAc) have negative effects on the TCH photooxidation, but the photocatalytic removal efficiency is still above 70%. The decreased removal efficiency of TCH is related to inorganic anions and organic matters acting as free radical scavengers [41]. Furthermore, negligible loss was found for the photooxidation of TCH in tap water. Environmental temperature can also affect the TCH photooxidation process [42]. Raising the temperature from 5 to 20 °C enhances TCH removal, attributed to the heightened thermodynamic driving force that accelerates chemical reactions during heterogeneous oxidation. However, further increasing the temperature to 60 °C, the removal rate slightly decreases. Elevated temperature can accelerate active species decomposition in solution, potentially counteracting thermal effects in heterogeneous oxidation.

$Z_{0.01}T/CNP$-4 photocatalyst has good stability and reusability. The stability was evaluated by 14 consecutive cycles under the same experimental conditions. After each cycle, the catalyst powder was collected by filtration, ethanol-washed to remove surface-bound organic molecules, oven-dried, and subsequently reused. Fig. 4d presents the results of the 14-cycle TCH photooxidation test under visible irradiation. In the 14th cycle, $Z_{0.01}T/CNP$-4 can remove 69% TCH within 20 min. More importantly, XRD, XPS, and SEM analyses demonstrate that the used catalyst after 14 cycles has the same phase structure, valence state, and morphology as the fresh one (Fig. 4e-g and Fig. S14). Based on the analysis, the excellent stability of the photocatalyst $Z_{0.01}T/CNP$-4, along with the feasibility of its synthesis process, holds great promise for practical applications.

3.4. TCH photooxidation pathways and toxicity evaluation

DFT calculations provide insight into the highest occupied molecular orbital (HOMO), the lowest unoccupied molecular orbital (LUMO), and the condensed Fukui index of the TC molecule. Calculating results reveal that active species attack the reaction sites of TC molecules over catalyst ZT/CNP. In Fig. 5a, the electron-rich and electron-poor regions are represented in blue and yellow areas, respectively. The parameter f^0 is
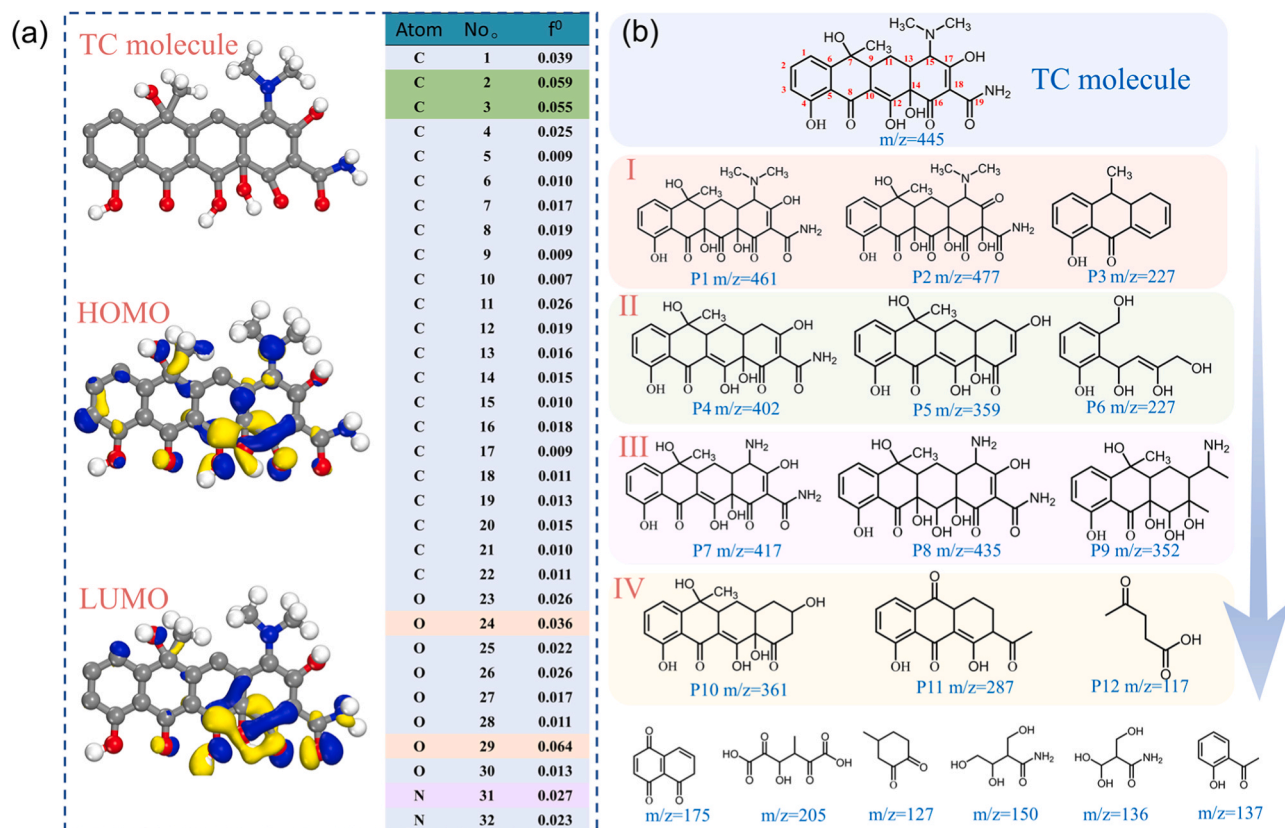
Fig. 5. Potential reaction pathway. (a) Chemical structure, HOMO, LUMO, and Fukui index of TC molecule, and (b) the possible degradation pathway for TC molecule by ZT/CNP photooxidation system.

the Fukui indices of susceptibility. Usually, the larger the value of f^0, the easier it is for the reaction site to be attacked. The C2 ($f^0 = 0.059$), C3 ($f^0 = 0.055$), O29 ($f^0 = 0.064$), O24 ($f^0 = 0.036$), and N31 ($f^0 = 0.027$) have high f^0 values and are susceptible to be attacked by reactive substances (h^+, $\bullet OH$, and $\bullet O_2$) in the reaction system [43–45]. Based on the results of DFT calculations and analysis of liquid chromatography-mass spectrometry (LC-MS), we propose four possible removal pathways. As shown in Fig. 5b and Fig. S15, functional groups with high electron density, such as double bonds, amine groups, and phenolic groups in TCH molecules, are easily attacked by reactive radicals, resulting in numerous intermediates (P1 to P12). In pathway I, the TCH molecule ($m/z = 445$) undergoes hydroxylation at the C10 position to convert into P1 ($m/z = 461$) and further at C18 to transform into P2 ($m/z = 477$). Both intermediates subsequently suffer oxidative ring-opening and carbon bond scission processes, leading to intermediate P3. In pathway II, the weak N-C bond in TCH is first attacked by free radicals, such as h^+, during photocatalysis. The cleavage of the N-C bond at the C10 position results in demethylation and the formation of intermediate P4 which further transforms into intermediates P5 and P6. For the pathway III process, the attack of $\bullet O_2$ and $\bullet OH$ directly causes the demethylation of TCH, producing P7 ($m/z = 417$). Subsequently, P7 is hydroxylated to yield P8 ($m/z = 435$), and P8 degrades to P9 ($m/z = 352$) through multi-step fragmentation, involving deamidation, dihydroxylation, and ring-opening processes. In pathway IV, active radicals attack TCH ($m/z = 445$), leading to deamination and dissociation of the dimethylamino group to form P10 ($m/z = 361$). P10 is further converted to P11 ($m/z = 286$) by a ring-opening reaction. Intermediate P11 is converted to P12 ($m/z = 117$) with further cleavage of the ring. Finally, the intermediates convert into small organic molecules ($m/z = 127$, 137, 150, and 175), as well as carbon dioxide, among others due to continuous attack and oxidation of active free radicals.

The biotoxicities of TCH and its intermediates were tested by the Toxicity Estimation Software Tool (T.E.S.T.) through quantitative structure-activity relationship modeling (QSAR) [46]. As depicted in Fig. 6a-c, the toxicity of the intermediates formed during TCH photooxidation was significantly reduced. Moreover, the developmental toxicity of most of the intermediates is lower than that of the original TCH solution. Overall, the removal of TCH by $Z_{0.01}T/CNP-4$ follows a gradual photooxidation process to generate various intermediates, and the further mineralization of these intermediates ensures their safety for the ecosystem.

The potential toxicity of $Z_{0.01}T/CNP-4$ photocatalyst and the photooxidation intermediates of TCH were evaluated based on their impact on the population density of surviving bacterial colonies, in comparison to a blank control group [47]. As shown in Fig. 6d, introducing $Z_{0.01}T/CNP-4$ leaching solution does not significantly reduce the bacterial colony density. In contrast, the original solution containing TCH molecules (0 min of photocatalytic treatment) substantially inhibits the growth of E. coli colonies. However, upon the addition of the photooxidation-treated solution, the growth of E. coli colonies resembles that of the blank group, indicating the effective photooxidation of TCH molecules by the catalyst $Z_{0.01}T/CNP-4$. These experimental observations align with the toxicity evaluation results of the photooxidation intermediates (Figs. 6a-6c, determined by toxicity estimation software).

3.5. Carrier transport mechanism

The photooxidation mechanism of TCH over $Z_{0.01}T/CNP-4$ can be revealed by both of quenching experiment and ESR analysis of radical species. Isopropanol (IPA), $AgNO_3$, triethanolamine (TEOA), and ascorbic acid (VC) were chosen as quenchers for $\bullet OH$, e^-, $h+$, and $\bullet O_2^-$, respectively. As depicted in Fig. 7a-b, all added quenchers have certain inhibition on TCH removal except for $AgNO_3$. In other words, $\bullet OH$ and e^-
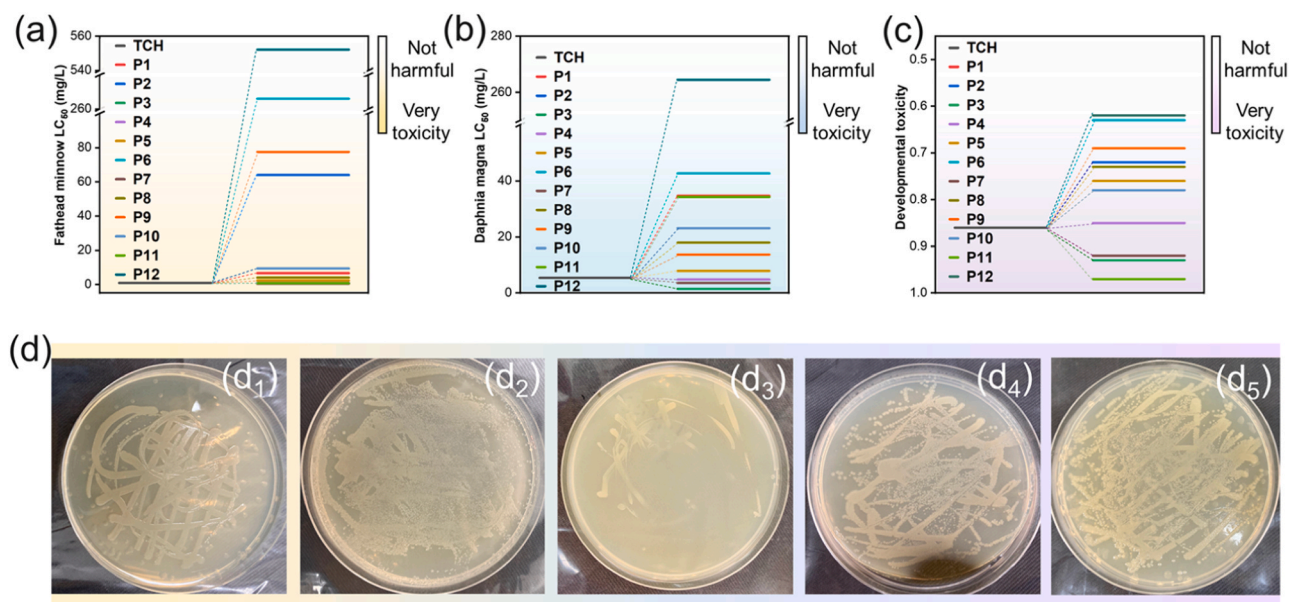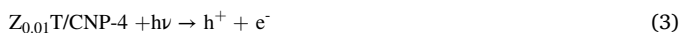
Fig. 6. Toxicity evaluation of TCH and the intermediates. (a) Fathead minnow LC_{50}, (b) Daphnia magna LC_{50}, and (c) development toxicity. (d) Photographs of E.coli colonies formed on LB-agar plates: (d_1) blank, (d_2) adding the leaching solution with catalyst $Z_{0.01}T/CNP-4$; (d_3) and (d_4) adding the photooxidation-treated solution after light irradiation of 0 min and 20 min, respectively; (d_5) no TCH solution was added.

are not the primary active species of TCH photooxidation, while h^+ and $^\bullet O_2^-$ as the main active species play a crucial role in the TCH removal. The quenching results of radical species were further investigated by ESR analysis using 5,5-dimethyl-1-pyrroline N-oxide (DMPO) and 2,2,6,6- tetramethylpiperidine (TEMP) as spin traps in the mixed solution of TCH and methanol (or water) [21,48]. Typical signals arising from DMPO-$^\bullet O_2^-$ and DMPO-$^\bullet OH$ were observed under visible light irradiation over $Z_{0.01}T/CNP-4$ (Fig. 7c-d), confirming the formation of radicals ($^\bullet O_2^-$ and $^\bullet OH$) in the photocatalytic reaction. Therefore, $h+$, $^\bullet OH$, and $^\bullet O_2^-$ are active species, and h^+ and $^\bullet O_2^-$ dominate the photooxidation reaction of TCH.

Combined with the XPS valence band spectrum (Fig. 7e) of sample $Zn_{0.01}Ti_{0.99}O_2$ and the Mott-Schottky curve (Fig. S16) of CNP, the energy band structure of $Z_{0.01}T/CNP-4$ is sketched, as shown in Fig. 7f. All potential values are versus RHE (reversible hydrogen electrode). The redox potential of $^\bullet O_2^-/H_2O_2$ is at 0.895 eV, above the VB of $Zn_{0.01}Ti_{0.99}O_2$. The generation of $^\bullet O_2^-$ from H_2O_2 is favorable in the photooxidation reaction of TCH. Two possible ways are responsible for the generation of H_2O_2: $2 H_2O + 2 h^+ \rightarrow H_2O_2 + 2 H^+$ and $2 H^+ + ^\bullet O_2 + 2e^- \rightarrow H_2O_2$. The redox potentials of H_2O_2/H_2O and O_2/H_2O_2 are 1.347 and 0.281 eV, respectively, i.e. both reactions can be initiated. The production of H_2O_2 is the vital step for the TCH photooxidation over $Z_{0.01}T/CNP-4$ to generate $^\bullet O_2^-$. Therefore, the TCH photooxidation over $Z_{0.01}T/CNP-4$ can be described as:

$$Z_{0.01}T/CNP-4 + h\nu \rightarrow h^+ + e^- \tag{3}$$

$$e^- + O_2 \rightarrow ^\bullet O_2^- \tag{4}$$

$$^\bullet O_2^- + H^+ \rightarrow ^\bullet HO_2 \rightarrow H_2O_2 \tag{5}$$

$$H_2O_2 + e^- \rightarrow ^\bullet OH + OH^- \tag{6}$$

$$^\bullet O_2^-/h^+/ ^\bullet OH + TCH \rightarrow Products \tag{7}$$

Equation (3) indicates that photogenerated electrons react with O_2 to yield H_2O_2, while the holes participate in the oxidation of TCH (Eq·5). To verify the generation of H_2O_2 during the TCH removal, we recorded the time-dependent absorbance spectra of H_2O_2 and the temporal evolution of H_2O_2 yield during the photooxidation process of TCH (Fig·S17) [21,49]. In the TCH removal reaction over $Z_{0.01}T/CNP-4$ catalyst, once photogenerated carriers are

separated, holes participate in the TCH photooxidation reaction, and electrons promote the generation of H_2O_2·These findings highlight the exceptional performance of sample $Z_{0.01}T/CNP-4$ in the photoreduction of O_2 to H_2O_2, which achieves efficient utilization of carriers and mitigates recombination effects·

4. Conclusion

In conclusion, we have successfully constructed an atomic scale p-n junction constructed by n-type semiconductors to enhance charge transportation. XANES, XPS, and Mott-Schottky analyses robustly reveal the charge separation and transfer due to the formation of the p-n junction. Free radical trapping experiments and ESR analysis demonstrate that $^\bullet O_2^-$, h^+ and $^\bullet OH$ radicals are the main active species during the photocatalytic reaction process. Moreover, the generation of H_2O_2 effectively consumes electrons, suppressing carrier recombination, while photoexcited hole carriers migrate to the catalyst's surface for the photooxidation reaction. The obtained photocatalyst $Z_{0.01}T/CNP-4$ effectively removes TCH with a high space-time yield. Even after 14 repeated cycles, sample $Z_{0.01}T/CNP-4$ maintains excellent stability. This study provides valuable insights into the design of novel photocatalysts featuring atomic-scale p-n junction, advancing the practical application of clean energy in environmental remediation.

CRediT authorship contribution statement

Li Liping: Conceptualization, Formal analysis, Writing – review & editing, Funding acquisition. **Li Guangshe:** Conceptualization, Funding acquisition, Supervision. **Wang Yan:** Data curation, Investigation, Methodology. **Fan Zhipeng:** Methodology. **Wang Jinghui:** Formal analysis. **Wang Yaowen:** Investigation, Methodology. **Liu Chang:** Data curation, Software, Writing – original draft, Writing – review & editing. **Shao Jingze:** Data curation, Methodology.

Declaration of Competing Interest

The authors declare that they have no known competing financial interests or personal relationships that could have appeared to influence the work reported in this paper.
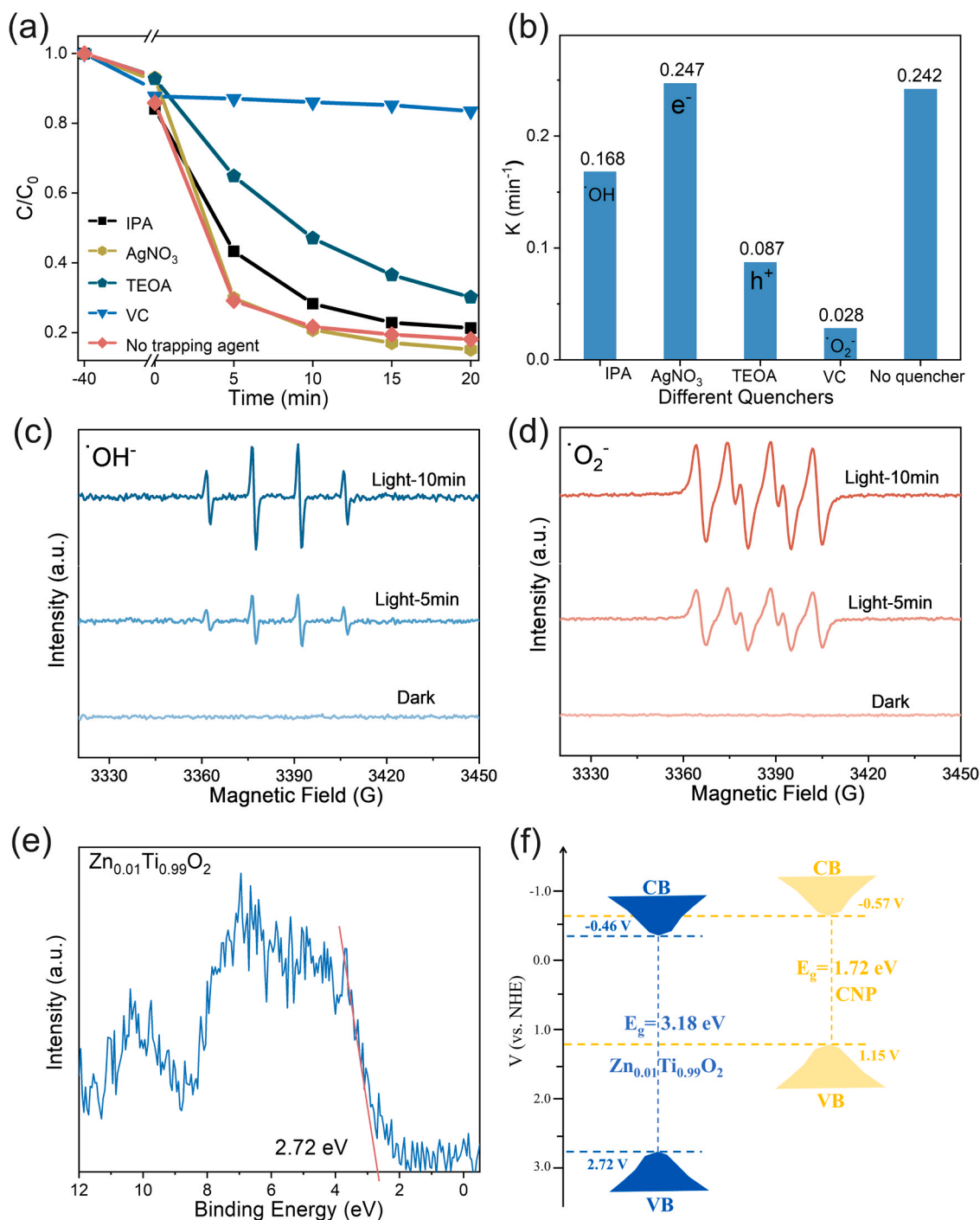
Fig. 7. Proposed reaction mechanism. TCH removal curves (a) over $Z_{0.01}T/CNP-4$ with different quenchers under visible light irradiation, and (b) corresponding rate constants. ESR signals for (c) DMPO-•OH, and (d) DMPO-•O_2^-. (e) XPS valence band spectrum of $Zn_{0.01}Ti_{0.99}O_2$, and (f) Scheme of energy band structure of $Z_{0.01}T/CNP-4$.

Data Availability

Data will be made available on request.

Acknowledgments

Appendix A. Supporting information

Supplementary data associated with this article can be found in the online version at doi:10.1016/j.apcatb.2023.123673.

References

[1] X. Li, C. Li, Y. Xu, Q. Liu, M. Bahri, L. Zhang, N.D. Browning, A.J. Cowan, J. Tang, Efficient hole abstraction for highly selective oxidative coupling of methane by Au-sputtered TiO$_2$ photocatalysts, Nat. Energy (2023) 1–10, https://doi.org/10.1038/s41560-023-01317-5.

[2] X. Li, C. Wang, J. Yang, Y. Xu, Y. Yang, J. Yu, J.J. Delgado, N. Martsinovich, X. Sun, X.-S. Zheng, W. Huang, J. Tang, PdCu nanoalloy decorated photocatalysts for efficient and selective oxidative coupling of methane in flow reactors, Nat. Commun. 14 (1) (2023) 6343, https://doi.org/10.1038/s41467-023-41996-y.

[3] B. Ran, L. Ran, Z. Wang, J. Liao, D. Li, K. Chen, W. Cai, J. Hou, X. Peng, Photocatalytic antimicrobials: principles, design strategies, and applications, Chem. Rev. (2023), https://doi.org/10.1021/acs.chemrev.3c00326.

[4] F. Guo, C. Mao, C. Liang, P. Xing, L. Yu, Y. Shi, S. Cao, F. Wang, X. Liu, Z. Ai, L. Zhang, Triangle Cl-Ag$_1$-Cl sites for superior photocatalytic molecular oxygen activation and NO oxidation of BiOCl, Angew. Chem. Int. Ed. (2023) e202314243, https://doi.org/10.1002/anie.202314243.

[5] S. Le, W. Li, Y. Wang, X. Jiang, X. Yang, X. Wang, Carbon dots sensitized ^{2}D–^{2}D heterojunction of BiVO$_4$/Bi$_3$TaO$_7$ for visible light photocatalytic removal towards the broad-spectrum antibiotics, J. Hazard. Mater. 376 (2019) 1–11, https://doi.org/10.1016/j.jhazmat.2019.04.088.

[6] Y. Bai, Y. Zhou, J. Zhang, X. Chen, Y. Zhang, J. Liu, J. Wang, F. Wang, C. Chen, C. Li, R. Li, C. Li, Homophase junction for promoting spatial charge separation in photocatalytic water splitting, ACS Catal. 9 (4) (2019) 3242–3252, https://doi.org/10.1021/acscatal.8b05050.

[7] Y. Xiao, C. Feng, J. Fu, F. Wang, C. Li, V.F. Kunzelmann, C.-M. Jiang, M. Nakabayashi, N. Shibata, I.D. Sharp, K. Domen, Y. Li, Band structure engineering and defect control of Ta$_3$N$_5$ for efficient photoelectrochemical water oxidation, Nat. Catal. 3 (11) (2020) 932–940, https://doi.org/10.1038/s41929-020-00522-9.

[8] W. Li, Y. Zhang, Y. Wang, W. Ran, Q. Guan, W. Yi, L. Zhang, D. Zhang, N. Li, T. Yan, Graphdiyne facilitates photocatalytic CO$_2$ hydrogenation into C$_{2+}$ hydrocarbons, Appl. Catal. B Environ. 340 (2024) 123267, https://doi.org/10.1016/j.apcatb.2023.123267.

[9] J. Lyu, J. Shao, Y. Wang, Y. Qiu, J. Li, T. Li, Y. Peng, F. Liu, Construction of a porous core-shell homojunction for the photocatalytic degradation of antibiotics, Chem. Eng. J. 358 (2019) 614–620, https://doi.org/10.1016/j.cej.2018.10.085.

[10] T. Tang, Z. Yin, J. Chen, S. Zhang, W. Sheng, W. Wei, Y. Xiao, Q. Shi, S. Cao, Novel p-n heterojunction Bi$_2$O$_3$/Ti^{3+}-TiO$_2$ photocatalyst enables the complete removal of tetracyclines under visible light, Chem. Eng. J. 417 (2021) 128058, https://doi.org/10.1016/j.cej.2020.128058.

[11] J. Ding, Z. Geng, L. Li, Y. Wang, Y. Zuo, H. Li, M. Yang, G. Li, Migration of cations in layered oxides for creating a highly active interface toward CO preferential oxidation, J. Mater. Chem. A 9 (21) (2021) 12623–12635, https://doi.org/10.1039/d0ta11762e.

[12] S. Wang, G. Li, T. Huang, C. Liu, X. Li, Q. Zhang, Y. Zou, L. Li, Exceptional high temperature interface chemistry: a creation of P-Sn bonds and enhanced photoreduction ability, Chem. Eng. J. 430 (2022) 132593, https://doi.org/10.1016/j.cej.2021.132593.

[13] G. Žerjav, K. Žižek, J. Zavašnik, A. Pintar, Brookite vs. rutile vs. anatase: what`s behind their various photocatalytic activities? J. Environ. Chem. Eng. 10 (3) (2022) 107722 https://doi.org/10.1016/j.jece.2022.107722.

[14] S. Cao, T.-S. Chan, Y.-R. Lu, X. Shi, B. Fu, Z. Wu, H. Li, K. Liu, S. Alzuabi, P. Cheng, M. Liu, T. Li, X. Chen, L. Piao, Photocatalytic pure water splitting with high efficiency and value by Pt/porous brookite TiO$_2$ nanoflutes, Nano Energy 67 (2020) 104287, https://doi.org/10.1016/j.nanoen.2019.104287.

[15] J.J.M. Vequizo, H. Matsunaga, T. Ishiku, S. Kamimura, T. Ohno, A. Yamakata, Trapping-induced enhancement of photocatalytic activity on brookite TiO$_2$ powders: comparison with anatase and rutile TiO$_2$ powders, ACS Catal. 7 (4) (2017) 2644–2651, https://doi.org/10.1021/acscatal.7b00131.

[16] J.-J. Li, S.-C. Cai, Z. Xu, X. Chen, J. Chen, H.-P. Jia, J. Chen, Solvothermal syntheses of Bi and Zn co-doped TiO$_2$ with enhanced electron-hole separation and efficient photodegradation of gaseous toluene under visible-light, J. Hazard. Mater. 325 (2017) 261–270, https://doi.org/10.1016/j.jhazmat.2016.12.004.

[17] Y. Zhu, C. Lv, Z. Yin, J. Ren, X. Yang, C.L. Dong, H. Liu, R. Cai, Y.C. Huang, W. Theis, S. Shen, D. Yang, A [001]-oriented Hittorf`s phosphorus nanorods/polymeric carbon nitride heterostructure for boosting wide-spectrum-responsive photocatalytic hydrogen evolution from pure water, Angew. Chem. Int. Ed. 59 (2) (2019) 868–873, https://doi.org/10.1002/anie.201911503.

[18] H. Shen, X. Zhan, S. Hong, A.W. Robertson, L. Hao, F. Fu, Z. Sun, Ultrafine MoO$_x$ clusters anchored on g-C$_3$N$_4$ with nitrogen/oxygen dual defects for synergistic efficient O$_2$ activation and tetracycline photodegradation, Nano Res. 16 (8) (2023) 10713–10723, https://doi.org/10.1007/s12274-023-5880-y.

[19] Y. Zang, L. Li, Y. Xu, Y. Zuo, G. Li, Hybridization of brookite TiO$_2$ with g-C$_3$N$_4$: a visible-light-driven photocatalyst for As^{3+} oxidation, MO degradation and water splitting for hydrogen evolution, J. Mater. Chem. A 2 (38) (2014) 15774–15780, https://doi.org/10.1039/c4ta02082k.

[20] M. Guo, L. Li, H. Lin, Y. Zuo, X. Huang, G. Li, Targeted deposition of ZnO$_2$ on brookite TiO$_2$ nanorods towards high photocatalytic activity, Chem. Commun. 49 (100) (2013) 11752–11754, https://doi.org/10.1039/c3cc47461e.

[21] J. Yue, H. Yang, C. Liu, Q. Zhang, Y. Ao, Constructing photocatalysis-self-Fenton system over a defective twin C$_3$N$_4$: In-situ producing H$_2$O$_2$ and mineralizing organic pollutants, Appl. Catal. B Environ. 331 (2023) 122716, https://doi.org/10.1016/j.apcatb.2023.122716.

[22] H. Lin, L. Li, M. Zhao, X. Huang, X. Chen, G. Li, R. Yu, Synthesis of high-quality brookite TiO$_2$ single-crystalline nanosheets with specific facets exposed: tuning

[23] L.L.Wanbiao Hu, Guangshe Li, Changlin Tang, Lang Sun, High-quality brookite TiO$_2$ flowers: synthesis, characterization, and dielectric performance, Cryst. GROWTH Des. 9 (2009) 3676–3682, https://doi.org/10.1021/cg9004032.

[24] X. Li, X. Wang, J. Ding, M. Ma, S. Yuan, Q. Yang, Z. Wang, Y. Peng, C. Sun, H. Zhou, H. Liu, Y.A. Wu, K. Huang, L. Li, G. Li, S. Feng, Engineering active surface oxygen sites of cubic perovskite cobalt oxides toward catalytic oxidation reactions, ACS Catal. 13 (9) (2023) 6338–6350, https://doi.org/10.1021/acscatal.3c00139.

[25] Q. Wang, L. Li, T. Huang, Q. Ding, D. Yu, L. Bu, B. Liang, H. Liu, G. Li, Sequencing the CuO$_x$ active species for CO preferential oxidation at low-temperature over CeO$_2$-CuO composite catalysts, Chem. Eng. J. 452 (2023) 139467, https://doi.org/10.1016/j.cej.2022.139467.

[26] Y. Zhang, J. Gao, Z. Chen, A solid-state chemical reduction approach to synthesize graphitic carbon nitride with tunable nitrogen defects for efficient visible-light photocatalytic hydrogen evolution, J. Colloid Interface Sci. 535 (2019) 331–340, https://doi.org/10.1016/j.jcis.2018.10.012.

[27] Y. Zhu, J. Ren, G. Huang, C.L. Dong, Y.C. Huang, P. Lu, H. Tang, Y. Liu, S. Shen, D. Yang, Red phosphorus grafted high-index (116) faceted anatase TiO$_2$ for Z-scheme photocatalytic pure water splitting, Adv. Funct. Mater. (2023) 2311623, https://doi.org/10.1002/adfm.202311623.

[28] H. Shen, C. Yang, W. Xue, L. Hao, D. Wang, F. Fu, Z. Sun, Construction of ternary bismuth-based heterojunction by using (BiO)$_2$CO$_3$ as electron bridge for highly efficient degradation of phenol, Chem. – A Eur. J. 29 (38) (2023) e202300748, https://doi.org/10.1002/chem.202300748.

[29] C. Liu, J. Shao, Y. Wang, Z. Geng, S. Wang, Y. Wang, L. Li, G. Li, Enhancing catalytic performance of TiO$_2$/P-doped C$_3$N$_4$ composite via preferentially bonded P-O-Ti, J. Alloy. Compd. 970 (2024) 172460, https://doi.org/10.1016/j.jallcom.2023.172460.

[30] X. Han, B. Lu, X. Huang, C. Liu, S. Chen, J. Chen, Z. Zeng, S. Deng, J. Wang, Novel p- and n-type S-scheme heterojunction photocatalyst for boosted CO$_2$ photoreduction activity, Appl. Catal. B: Environ. 316 (2022) 121587, https://doi.org/10.1016/j.apcatb.2022.121587.

[31] Z. Ai, Y. Shao, B. Chang, L. Zhang, J. Shen, Y. Wu, B. Huang, X. Hao, Rational modulation of p-n homojunction in P-doped g-C$_3$N$_4$ decorated with Ti$_3$C$_2$ for photocatalytic overall water splitting, Appl. Catal. B Environ. 259 (2019) 118077, https://doi.org/10.1016/j.apcatb.2019.118077.

[32] Y. Liao, G. Wang, J. Wang, K. Wang, S. Yan, Y. Su, Nitrogen vacancy induced in situ g-C$_3$N$_4$ p-n homojunction for boosting visible light-driven hydrogen evolution, J. Colloid Interface Sci. 587 (2021) 110–120, https://doi.org/10.1016/j.jcis.2020.12.009.

[33] L. Li, R. Zhang, Y. Lin, D. Wang, T. Xie, Plasmon-enhanced bulk charge separation via morphological and interfacial engineering in Au@carbon dots@CdS hybrid, Chem. Eng. J. 453 (2023), https://doi.org/10.1016/j.cej.2022.139970.

[34] T. Jiang, T. Xie, W. Yang, L. Chen, H. Fan, D. Wang, Photoelectrochemical and photovoltaic properties of p–n Cu$_2$O homojunction films and their photocatalytic performance, J. Phys. Chem. C 117 (9) (2013) 4619–4624, https://doi.org/10.1021/jp311532s.

[35] G. Liu, G. Zhao, W. Zhou, Y. Liu, H. Pang, H. Zhang, D. Hao, X. Meng, P. Li, T. Kako, J. Ye, In situ bond modulation of graphitic carbon nitride to construct p-n homojunctions for enhanced photocatalytic hydrogen production, Adv. Funct. Mater. 26 (37) (2016) 6822–6829, https://doi.org/10.1002/adfm.201602779.

[36] K. Zhang, D.D. Deng, B. Zheng, Y. Wang, F.K. Perkins, N.C. Briggs, V.H. Crespi, J. A. Robinson, Tuning transport and chemical sensitivity via niobium doping of synthetic MoS$_2$, Adv. Mater. Interfaces 7 (18) (2020), https://doi.org/10.1002/admi.202000856.

[37] L. Liao, X. Ding, J. Li, L. Huang, M. Zhang, Y. Fan, X. Zhou, Y. Zhang, S. Mo, Q. Xie, D. Ye, Constructing MOFs-derived Co$_3$O$_4$ microsphere with atomic p-n homojunction as an efficient photothermal catalyst for boosting ethyl acetate oxidation under light irradiation, Sep. Purif. Technol. 309 (2023), https://doi.org/10.1016/j.seppur.2022.122939.

[38] X. He, T. Kai, P. Ding, Heterojunction photocatalysts for degradation of the tetracycline antibiotic: a review, Environ. Chem. Lett. 19 (6) (2021) 4563–4601, https://doi.org/10.1007/s10311-021-01295-8.

[39] L. Luo, S. Dong, H. Chen, H. Jin, T. Huang, Construction of MgIn$_2$S$_4$/ZnIn$_2$S$_4$ micro-flowers: efficient degradation of tetracycline hydrochloride over a wide pH range, Appl. Surf. Sci. 581 (2022) 152417, https://doi.org/10.1016/j.apsusc.2021.152417.

[40] M. Abinaya, K. Govindan, M. Kalpana, K. Saravanakumar, S.L. Prabavathi, V. Muthuraj, A. Jang, Reduction of hexavalent chromium and degradation of tetracycline using a novel indium-doped Mn$_2$O$_3$ nanorod photocatalyst, J. Hazard. Mater. 397 (2020) 122885, https://doi.org/10.1016/j.jhazmat.2020.122885.

[41] Y. Luo, A. Zheng, J. Li, Y. Han, M. Xue, L. Zhang, Z. Yin, C. Xie, Z. Chen, L. Ji, Z. Hong, X. Xie, Integrated adsorption and photodegradation of tetracycline by bismuth oxycarbonate/biochar nanocomposites, Chem. Eng. J. 457 (2023) 141228, https://doi.org/10.1016/j.cej.2022.141228.

[42] T. Lu, Y. Gao, Y. Yang, H. Ming, Z. Huang, G. Liu, D. Zheng, J. Zhang, Y. Hou, Efficient degradation of tetracycline hydrochloride by photocatalytic ozonation over Bi$_2$WO$_6$, Chemosphere 283 (2021) 131256, https://doi.org/10.1016/j.chemosphere.2021.131256.

[43] B. Li, F. Tong, M. Lv, Z. Wang, Y. Liu, P. Wang, H. Cheng, Y. Dai, Z. Zheng, B. Huang, In situ monitoring charge transfer on topotactic epitaxial heterointerface for tetracycline degradation at the single-particle level, ACS Catal. 12 (15) (2022) 9114–9124, https://doi.org/10.1021/acscatal.2c02447.

[44] Q. Chen, H. Zhou, J. Wang, J. Bi, F. Dong, Activating earth-abundant insulator BaSO$_4$ for visible-light induced degradation of tetracycline, Appl. Catal. B: Environ. 307 (2022) 121182, https://doi.org/10.1016/j.apcatb.2022.121182.

[45] Y. Sun, W. Wu, H. Zhou, Lignosulfonate-controlled BiOBr/C hollow microsphere photocatalyst for efficient removal of tetracycline and Cr(VI) under visible light, Chem. Eng. J. 453 (2023) 139819, https://doi.org/10.1016/j.cej.2022.139819.

[46] X. Shen, B. Song, X. Shen, C. Shen, S. Shan, Q. Xue, X. Chen, S. Li, Rationally designed S-scheme heterojunction of C$_3$N$_4$/Bi$_2$MoO$_6$/carbon fiber cloth as a recyclable, macroscopic and efficient photocatalyst for wastewater treatment, Chem. Eng. J. 445 (2022) 136703, https://doi.org/10.1016/j.cej.2022.136703.

[47] J. Guo, H. Sun, X. Yuan, L. Jiang, Z. Wu, H. Yu, N. Tang, M. Yu, M. Yan, J. Liang, Photocatalytic degradation of persistent organic pollutants by Co-Cl bond reinforced CoAl-LDH/Bi$_{12}$O$_{17}$Cl$_2$ photocatalyst: mechanism and application prospect evaluation, Water Res. 219 (2022) 118558, https://doi.org/10.1016/j.watres.2022.118558.

[48] C. Li, Y. Zhao, Y. Song, X. Qiu, S. Wang, P. Sun, Optimization of electron transport pathway: a novel strategy to solve the photocorrosion of Ag-based photocatalysts, Environ. Sci. Technol. (2023), https://doi.org/10.1021/acs.est.2c07012.

[49] Y. Deng, J. Liu, Y. Huang, M. Ma, K. Liu, X. Dou, Z. Wang, S. Qu, Z. Wang, Engineering the photocatalytic behaviors of g/C$_3$N$_4$-based metal-free materials for degradation of a representative antibiotic, Adv. Funct. Mater. 30 (31) (2020) 2002353, https://doi.org/10.1002/adfm.202002353.